Voltage Control Method with Non-linear Compensation and DC-Offset Elimination for One-leg T-type Dual Active Bridge Converter using Multi-Operation Mode

Hayato Higa
Power Electronics Research Department
MEIDENSHA CORPORATION
Numazu, Shizuoka, Japan
higa-h@mb.meidensha.co.jp

Hiroki Watanebe, Keisuke Kusaka and Jun-ichi Itoh
Dept. of Electric Engineering
Nagaoka University of Technology
Nagaoka, Niigata, Japan
hwatanabe@vos.nagaokaut.ac.jp,
kusaka@vos.nagaokaut.ac.jp, itoh@vos.nagaokaut.ac.jp

Abstract*—This paper proposes a voltage control method for one-leg T-type Dual Active Bridge (TDAB) converter in order to achieve a linearization of a current-control characteristic and an elimination of a dc offset in a inductor current at a transient state. In the conventional Dual Active Bridge (DAB) converter, the controller design is complicated due to the nonlinearity of the current-control characteristic and the dc offset of the inductor current at the phase-shift angle and the operation mode changing. In the proposed method, the nonlinearity of the current-control characteristic is compensated by the reverse system model including the inductance error. In addition, the dc offset of the inductor current is eliminated by updating the phase-shift angle and changing the operation mode at the peak or bottom of the base carrier. From experimental results, the ratio between the output current command and the actual output current agrees with the ratio between the nominal value and the error value of the inductance, i.e. the maximum error of 8.8%. Moreover, the dc offset of the inductor current is prevented when the phase-shift angle and the operation modes are changed.

Keywords—Dual Active Bridge Converter; DC-offset elimination; Voltage Control Method

I. INTRODUCTION

Recently, a dc micro grid has been proposed for high system efficiency [1-4]. This system has numerous isolated dc-dc converters which have various demands such as a galvanic isolation, a wide dc voltage variation, a voltage control, a high efficiency in wide load and a bi-directional operation. A DAB converter achieves the high efficiency when the input and the output dc voltage are close to the rated voltage condition because zero voltage switching (ZVS) is achieved without additional components [5-6]. However, the converter efficiency is drastically decreased during the fluctuation of the input or the output dc voltage due to the hard switching operation and the increase of the inductor current [7-8].

In order to improve the converter efficiency against wide voltage variations, multi-level DAB converter using a TDAB converter [9-10] or a one-leg TDAB converter [11-13] with multi-mode operation have been proposed. However, the nonlinearity on the phase-shift angle to the output current occurs in the current-control characteristic of the multi-level DAB converter. As a result, the controller design is complicated because the transient response is varied in accordance with the operation point or the operation mode. Furthermore, the dc offset of the inductor current occurs when the phase-shift angle and the operation modes are changed. This dc offset of the inductor current is increased by the difference between the previous value and the current value of the phase-shift angle. Therefore, the change in the amount of phase-shift angle is limited in order to prevent the magnetic-flux saturation, i.e. the controller gain has to be designed to be low.

This paper proposes a voltage control method with a non-linear compensation and a dc-offset elimination in a transformer current for a one-leg TDAB converter. In the one-leg TDAB converter, two operation modes are changed as to improve the efficiency in wide load and output dc voltage variation. The proposed voltage control method has following features; the linearization of the current-control characteristic including the inductance error regardless of operation modes and the dc-offset elimination in the transformer current at the transient state. Consequently, the new contribution of this paper is the voltage control method with the simple controller design. This paper is organized as follows; first, the circuit configuration and the operation principle of the each operation mode are explained. Second, the nonlinearity compensation and the dc-offset elimination methods are introduced. Finally, a 1.5-kW prototype is demonstrated by the experiment at several voltage conditions in order to confirm the validity of the proposed voltage control method.

II. CIRCUIT CONFIGURATION AND OPERATION PRINCEPLE OF ONE-LEG TDAB CONVERTER

A. Circuit configulation

Fig. 1 shows the circuit configuration of the one-leg TDAB converter. The one-leg TDAB converter consists of the DAB converter, a bidirectional switch S_{ucp}, S_{ucn}, a high frequency transformer, an external inductance L_{ex}, and two capacitors C_p and C_n which capacitance are same capacitors.

Fig. 2 shows the operation modes of the one-leg TDAB converter. A Full bridge (FB) mode and a half bridge (HB) mode are changed on the input side as shown in Fig. 2 (a) and (b).

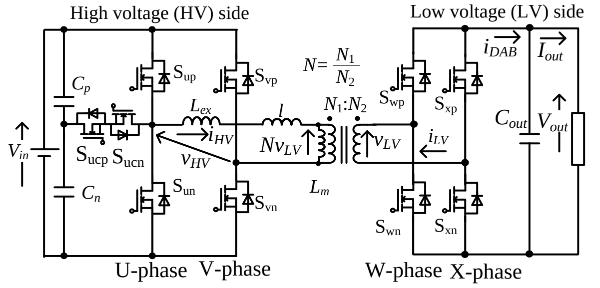

Fig. 1. Configuration of one-leg TDAB converter.

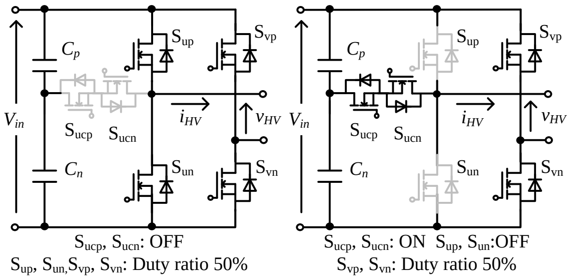

(a) Full bridge (FB) mode (b) Half bridge (HB) mode

Fig. 2. Switching patterns of FB and HB mode.

B. Operation analysis with each operation mode

Fig. 3 shows the operation waveforms of the one-leg TDAB converter. In both HB and FB mode, the output voltage v_{HV} and Nv_{LV} are square waveforms which have two voltage amplitude, i.e. FB mode; $\pm V_{in}$, HB mode; $\pm V_{in}/2$. Thus, the theoretical equations of the each operation mode are derived in the same manner with a conventional DAB converter. The direction of the power transfer is controlled by the phase difference δ between the HV- and LV-side inverters. There are four patterns in each switching period. As shown in Fig. 3(a) and 3(b), For the sake of brevity, only patterns I and II are considered here because the patterns III and IV are analyzed in the same manner. It should be noted that the magnetizing current is neglected because the total inductance of the leakage inductance l and the external inductance L_{ex} is much smaller than the magnetizing inductance L_m. In FB and HB modes, the inductor current during pattern I and pattern II $i_{HV\_FB\_I}$, $i_{HV\_FB\_II}$, $i_{HV\_HB\_I}$, $i_{HV\_HB\_II}$ are calculated as

FB mode Pattern I :($0 < \theta < \delta$)

$$i_{HV\_FB\_I}(\theta) = i_{HV\_FB}(0) + \frac{(V_{in} + NV_{out})}{\omega L}\theta \qquad (1),$$

FB mode Pattern II :($\delta < \theta < \pi$)

$$i_{HV\_FB\_II}(\theta) = i_{FB\_HV\_I}(\delta) + \frac{(V_{in} - NV_{out})}{\omega L}(\theta - \delta) \qquad (2),$$

HB mode Pattern I :($0 < \theta < \delta$)

$$i_{HV\_HB\_I}(\theta) = i_{HV\_HB}(0) + \frac{(V_{in}/2 + NV_{out})}{\omega L}\theta \qquad (3),$$

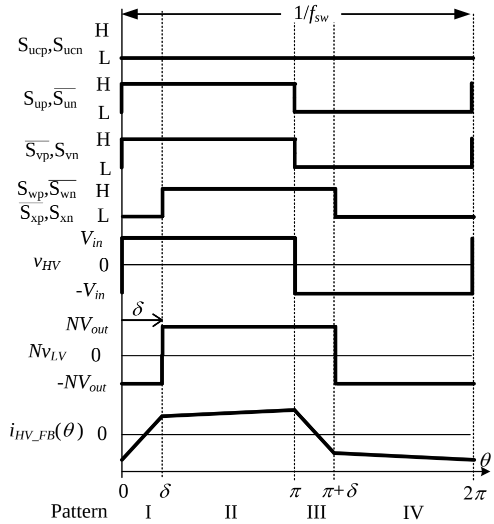

(a) FB mode (Power flow is HV side to LV side.)

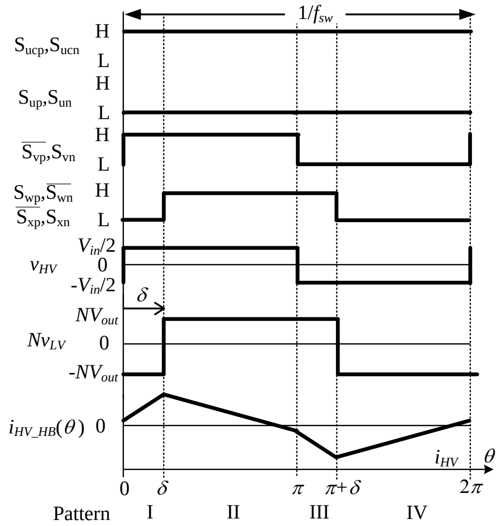

(b) HB mode (Power flow is HV side to LV side.)

Fig. 3. Operation waveforms of FB mode and HB mode

HB mode Pattern II :($\delta < \theta < \pi$)

$$i_{HV\_HB\_II}(\theta) = i_{HV\_HB\_I}(\delta) + \frac{(V_{in}/2 - NV_{out})(\theta - \delta)}{\omega L} \qquad (4)$$

where δ is the phase shift angle between the HV- and LV- side inverters, V_{in} is the dc voltage of the input side, V_{out} is the dc voltage of the load side, ω is the angular frequency of the switching frequency and L is the total inductance of the external inductance L_{ex} and the leakage inductance l. In Fig. 3, the absolute values of $i_{HV\_FB\_II}$ (π) and $i_{HV\_HB\_II}$ (π) are equal to that of $i_{HV\_FB\_I}$ (0) and $i_{HV\_FB\_I}$ (0), respecitively. Thus, the initial value of the inductor current $i_{HV\_FB\_I}$ (0) and $i_{HV\_HB\_I}$ (0) are calculated by (5) and (6).

$$i_{HV\_FB}(0) = -i_{HV\_FB\_II}(\pi) = -\frac{1}{\omega L}\left\{NV_{out}\delta + (V_{in} - NV_{out})\frac{\pi}{2}\right\} \quad (5)$$

$$i_{HV\_HB}(0) = -i_{HV\_HB\_II}(\pi) = -\frac{1}{\omega L}\left\{NV_{out}\delta + (V_{in}/2 - NV_{out})\frac{\pi}{2}\right\} \quad (6)$$

By substuting (5) and (6) into (1) and (3), the inductor current values of the pattern I with the each operation mode $i_{HV\_FB\_I}(\delta)$ and $i_{HV\_FB\_I}(\delta)$ are calculated by (7) and (8).

$$i_{HV\_FB\_I}(\delta) = i_{HV\_FB}(0) + \frac{(V_{in} + NV_{out})}{\omega L}\delta = \frac{1}{\omega L}\left\{V_{in}\delta - (V_{in} - NV_{out})\frac{\pi}{2}\right\} \quad (7)$$

$$i_{HV\_HB\_I}(\delta) = i_{HV\_HB}(0) + \frac{(V_{in}/2 + NV_{out})}{\omega L}\delta = \frac{1}{\omega L}\left\{V_{in}/2\delta - (V_{in}/2 - NV_{out})\frac{\pi}{2}\right\} \quad (8)$$

In addition, the root mean square (RMS) value of the inductor current with each operation mode I_{HV_FB} and I_{HV_HB} are determined by (9) and (10) [11].

$$I_{HV\_FB} = \sqrt{\frac{1}{\pi}\int_0^{\pi}\left\{i_{HV\_FB}(\theta)\right\}^2 d\theta} = \sqrt{\frac{1}{\pi}\left[\int_0^{\delta}\left\{i_{HV\_FB\_I}(\theta)\right\}^2 d\theta + \int_{\delta}^{\pi}\left\{i_{HV\_FB\_II}(\theta)\right\}^2 d\theta\right]} = \frac{\sqrt{NV_{in}V_{out}}}{\omega L}\sqrt{-\frac{2}{3\pi}\delta^3 + \delta^2 + \frac{\pi^2}{12}\frac{(V_{in} - NV_{out})^2}{NV_{in}V_{out}}} \quad (9)$$

$$I_{HV\_HB} = \sqrt{\frac{1}{\pi}\int_0^{\pi}\left\{i_{HV\_HB}(\theta)\right\}^2 d\theta} = \frac{\sqrt{NV_{out}V_{in}}}{\omega L}\sqrt{-\frac{\delta^3}{3\pi} + \frac{\delta^2}{2} + \frac{\pi^2}{12}\frac{\left(V_{in}/2 - NV_{out}\right)^2}{NV_{out}V_{in}}} \quad (10)$$

In FB mode, the inductor current is minimized at the voltage condition of $V_{in} = NV_{out}$, whereas the inductor current of HB mode is minimized at the voltage condition of $V_{in} / 2 = NV_{out}$. Besides, the ZVS condition is determined by the inductor current which is varied by the phase-shift angle and the voltage conditions [7]. In addition, ZVS is achieved in the same manner of the conventional DAB converter. Thus, the ZVS conditions in each operation mode are shown in phase-shift angle as (11) and (12) [11].

$$\text{FB mode}\begin{cases} \delta > \left(1 - \dfrac{NV_{out}}{V_{in}}\right)\dfrac{\pi}{2} & : V_{in} \geq NV_{out} \\ \delta > \left(1 - \dfrac{V_{in}}{NV_{out}}\right)\dfrac{\pi}{2} & : V_{in} \leq NV_{out} \end{cases} \quad (11)$$

$$\text{HB mode}\begin{cases} \delta > \left(1 - \dfrac{NV_{out}}{V_{in}/2}\right)\dfrac{\pi}{2} & : V_{in}/2 \geq NV_{out} \\ \delta > \left(1 - \dfrac{V_{in}/2}{NV_{out}}\right)\dfrac{\pi}{2} & : V_{in}/2 \leq NV_{out} \end{cases} \quad (12)$$

The ZVS range of HB mode is wide when the voltage ratio V_{in} / NV_{out} is close to 0.5. Besides, the ZVS range of HB mode is wide when the voltage ratio V_{in} / NV_{out} is close to 1.0. Accordingly, two operation modes are switched in accordance with the input and the output dc voltage condition and the transferred power to achieve the high efficiency in wide load. Then, the transferred powers in each operation mode P_{tr_FB} and P_{tr_HB} are calculated by the phase shift angle between the input-side inverter and the load-side inverter δ as (13) and (14) [11].

$$P_{tr\_FB} = \frac{NV_{in}V_{out}}{\omega L}\delta\left\{1 - \frac{|\delta|}{\pi}\right\} \quad (13)$$

$$P_{tr\_HB} = \frac{NV_{in}V_{out}}{2\omega L}\delta\left\{1 - \frac{|\delta|}{\pi}\right\} \quad (14)$$

According to (13) and (14), the transferred power of HB mode is lower than that of FB mode.

III. VOLTAGE CONTROL METHOD WITH LINEARIZATION AND DC-OFFSET ELIMINATION

A. Non-linear compensation

Fig. 4 shows control block diagrams of one-leg TDAB converter. In the power flow from HV side to LV side, i.e. δ>0, the output current of each operation mode are calculated by dividing (13) and (14) by the output voltage V_{out}. As a result, the output current of each operation mode i_{DAB_out} are expressed as

$$i_{DAB\_out} = \frac{P_{tr}}{V_{out}} = \frac{K_m NV_{in}}{\omega L}\left\{\delta - \frac{\delta^2}{\pi}\right\} \quad (15),$$

where K_m is coefficient which is decided by the operation modes. The coefficient K_m is 0.5 and 1.0 with HB mode and FB mode, respectively.

The transfer function of the current-control characteristic in the one-leg TDAB converter G_{DAB} is established in Fig. 4(a). In (15), the transfer function of the current-control characteristic in the one-leg TDAB converter G_{DAB} has the nonlinearity because G_{DAB} changes according to the phase-shift angle. This worsens the voltage response when PI controller is applied.

Therefore, the output of the PI controller is necessary to be compensated. In order to compensate the nonlinearity of one-leg TDAB converter, the phase-shift angle δ is calculated by (16) to match the output current in two modes.

$$\delta = \frac{\pi}{2}\left\{1-\sqrt{1-\frac{8 f_{sw} L \left| i_{DAB\_in} \right|}{K_m N V_{in}}}\right\} \tag{16}$$

where i_{DAB_in} is the output current command of the one leg TDAB converter.

The control block diagram in the one-leg TDAB converter is established in Fig. 4(b). By using (16), the one-leg TDAB converter's nonlinearity is eliminated over entire range. However, the actual inductance L_{act} might be different from the nominal value L. If the phase-shift angle-to-current transfer function has the inductance error ratio $k_{er}=L_{act}/L$, which is defined by substituting (15) into (16). The current of controller side to current-transfer function G_c is expressed as

$$G_c = \frac{i_{DAB\_out\_FB}}{i_{DAB\_in\_FB}} = \frac{i_{DAB\_out\_HB}}{i_{DAB\_in\_HB}} = 1/k_{er} \tag{17}.$$

According to (17), the transfer function G_c is determined by only the inductance error ratio k_{er}. As a result, the one-leg TDAB converter nonlinearity is eliminated by using the reverse system model regardless of the operation mode and the inductance error.

B. Dc offset in inductor current at operation mode changing

Fig. 5 shows the transient waveform at the conventional operation mode changing. The dc offset of the inductor current might occur when the operation mode and the phase-shift angle are changed. The dc offset of the inductor current is increased by the difference between the previous value and the current value of the phase-shift angle. The dc offset of the inductor current causes the increase of current rating devices and saturation of magnetic flux in the magnetic component, e.g. the external inductance and the high frequency transformer. Furthermore, the dc offset of the inductor current also occurs at the phase-shift angle changing [14]. The following switching sequence eliminates the dc offset of the inductor current at the phase-shift angle and the operation mode changing.

C. Proposed DC-offset elimination method

Fig. 6 shows the transient waveform at the operation mode and phase-shift angle changing. In order to eliminate the dc offset of the inductor current at the operation mode changing, The operation-mode-changing timing θ_{ch} is calculated by (18) when the instantaneous value of the inductor current with FB mode is equal to that with HB mode.

$$\begin{aligned} & i_{HV\_FB\_II}(\theta_{ch}) = i_{HV\_HB\_II}(\theta_{ch}) \\ & \theta_{ch} = \frac{\pi}{2} \end{aligned} \tag{18}$$

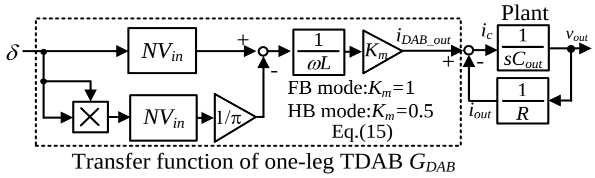

(a) Block diagram for one-leg TDAB converter

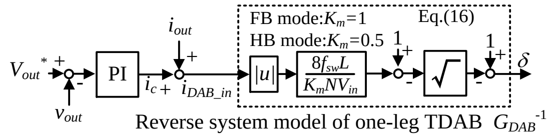

(b) Control block diagram

Fig. 4. Circuit and control block diagrams of one-leg TDAB converter. In Fig. 4(a), the current-control characteristic has a nonlinearlity. This leads the contlloer design is complicated due to changing the transfer function G_{DAB}. In Fig. .4 (b), the nonliniality compensation is applied by using the reverse system model.

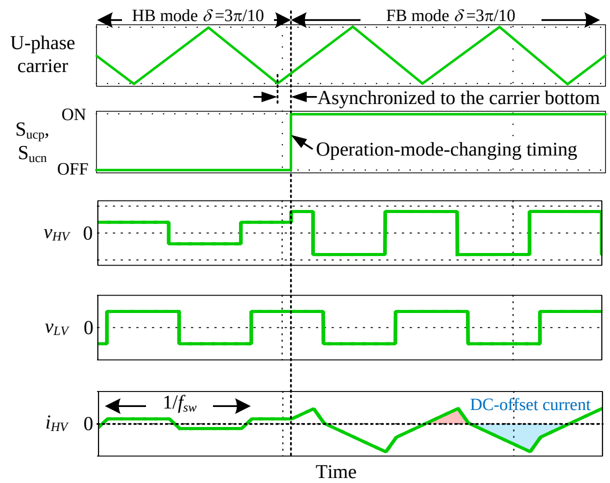

Fig. 5. Conventional operation mode changing at asynchronous U-phase carrier peak. The dc offset of the inductor current occurs. The dc-offset value is in accordance with the operation-mode-changing timing.

By (18), the operation-mode-changing timing is synchronized with the peak of U-phase carrier as shown at the timing B in Fig. 6. In order to realize the phase-shift-angle commend, the phase-shift carriers for each side are controlled independently. In the both HV- and LV- carrier, the V-phase are shifted by leading half of the phase-shift angle command $\delta/2$, whereas the X-phase carrier are shifted by lagging $\delta/2$ based on the base carrier. On the other hands, the U-phase are shifted by leading $\delta/2$, whereas W-phase carrier are shifted by lagging $\delta/2$ based on the base carrier. In order to eliminate DC-offset of inductor current at the phase-shift angle changing, the phase-shift command of each carrier is updated into two times as shown in timing A and C in Fig. 6 because the increment of the inductor current is reduced by inserting the zero voltage periods. Therefore, the detection of the inductor current is not necessary to eliminate the dc offset of the inductor current when changing the phase-shift angle and the operation mode.

D. Control block diagram with proposed method

Fig. 7 shows the control block diagram with the proposed voltage control method. The proposed voltage control method has the output current of each operation mode is matched at the changing timing of the operation mode. The operation-mode – changing flag (Flag_HB) is changed by the relationship between the threshold value and the load current. The threshold value is calculated by the loss calculation of each operation mode against the voltage condition. In addition, the threshold value has the hysteresis width I_{thp} and I_{thn} to avoid the chattering between FB mode and HB mode. Besides, the phase-shift angle is controlled by the phase-shift carrier which employs the elimination method of the dc offset of the inductor current at the load step change in individual operation mode [14]. Besides, the duty command d_{com} is set to half of the carrier peak $crpk/2$.

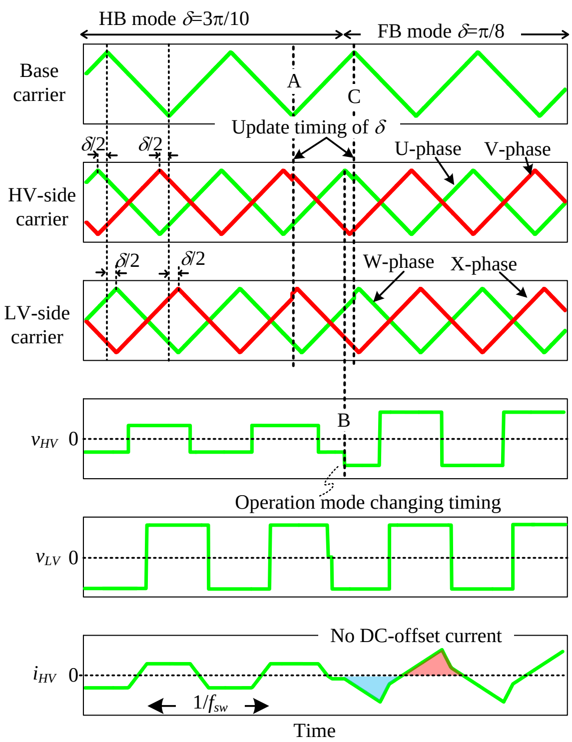

Fig. 6. Proposed operation mode and phase-shift changing at synchronous U-phase carrier peak. The dc offset in the inductor current does not occur when the operation mode is changed at U-phase-carrier peak as shown at the timing B. In addition, the phase-shift angle is updated into two steps of the peak and bottom of the base carrier as shown at the timing A and C.

IV. Experimental Results

A. Laboratory setup

The experimental results are demonstrated in order to evaluate the voltage control method for the one-leg TDAB converter by using experimental conditions as shown in Table 1. A 1.5-kW prototype (SCH2080KE which is SiC-MOSFET used at the input side and SCT3030AL which is SiC-MOSFET used at the load side, Rohm Semiconductor) is operated at the switching frequency of 80 kHz, the input voltage of 400 V, the load voltage of 200 V to 100 V. In addition, the inductance error ratio of k_{er} = 0.8 to 1.2, and the threshold values I_{thp}, and I_{thn} are 5 A and 4 A. In the operation mode changing, the dead-time between the bi-directional switches S_{ucp}, and S_{ucn} and the arm switches S_{up}, and S_{un} is set to 125 ns in order to prevent the short circuit. It should be noted that the dead-time error in the phase-shift angle occurs in the hard switching operation [14]. In order to compensate the dead-time error, the dead-time-error compensation method [14] is applied in the experimental set up.

B. Stadey state operation

Fig. 8 shows the operation waveform with FB mode at the rated power and the input voltage of 400 V and the output voltage of 200 V, i.e. the rated voltage condition. The rated power operation is confirmed by the experiment.

Fig. 9 shows the operation waveform with FB mode and HB mode at V_{in} = 400 V and V_{out}=100 V, i.e. NV_{out} / V_{in} = 0.5. In Fig. 9(a) and (b), the amplitude of inverter output voltage is changed. In addition, the inductor current of HB mode is smaller compared with that of FB mode. Consequently, the inductor current at the light load of 350 W (0.23 p.u.) is reduced by 39.5%.

Fig. 10 shows the output current characteristics of the

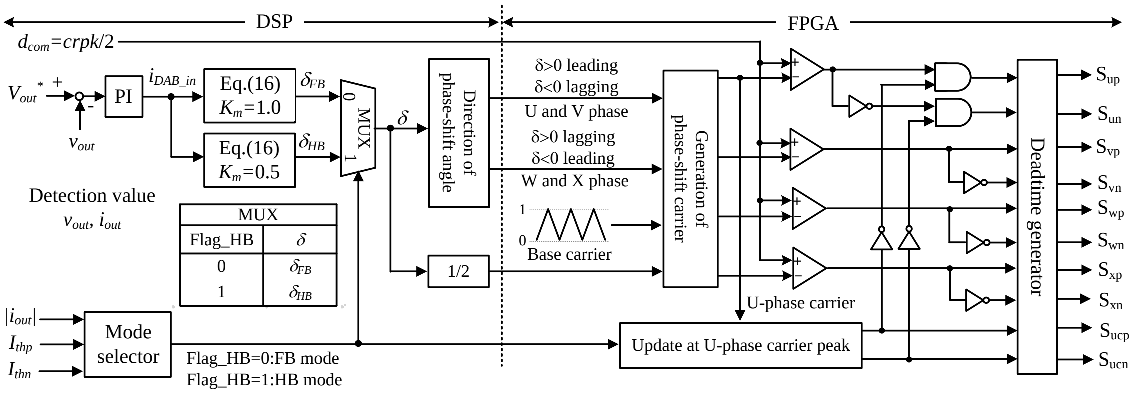

Fig. 7. Control block diagram with changing operation mode. In order to change the operation mode smoothly, the load current of each mode is matched at the changing timing of the operation mode. In the operation mode changing, the threshold value has the hysteresis width I_{thp} and I_{thn} to avoid the chattering between FB mode and HB mode.

Table I. Experimental conditions.

Element	Symbol	Value
Rated power	P_{rated}	1.5 kW@V_{out}=200 V
DC voltage in HV side	V_{in}	400 V
DC voltage in LV side	V_{out}	200 V, 100V
Dead time at HV side	T_{d_HV}	125 ns
Dead time at LV side	T_{d_LV}	100 ns
External inductance	L_{ex}	101 μH
Leakage inductance	l	23.1 μH
Magnetizing inductance	L_m	10.8 mH
Swiching frequency	f_{sw}	80 kHz
Sampling frequency	f_{samp}	20 kHz
Propotional gain	K_p	0.2 A/V
Integral time	T_i	100 ms
Output capacitance	C_{out}	40 μF
Unit capacitance constant [15]	H	267 μs @V_{out}=100 V, P_{out}=750 W
Threshold output current for switching operation mode		4.5 A ± 0.5 A(Hysteresis width)
Transformer		HV side: Litz wire ϕ0.1*150 LV side: Litz wire ϕ0.1*150*2 N87 ETD 59 (EPCOS) N_1:N_2=38:19
External Inductor		Litz wire ϕ0.1*150 N87 ETD 59 (EPCOS) Gap: 2.5 mm, Turn number: 23

calculation and experimental results. Fig. 10(a) shows the FB mode results, whereas Fig. 10(b) shows the HB mode results. In Fig. 10(a) and (b), the ratio between the output current command and the actual output current agrees with the inductance error ratio, i.e. the maximum error of 8.8%. This error is caused by the phase shift angle error due to the incomplete ZVS [16]. As a result, it is confirmed that the linearization of the current-control characteristics including the inductance error regardless of the operation mode.

Fig. 11 shows the efficiency characteristics with each operation mode. In Fig. 11(a), the maximum efficiency of 97.9% is achieved. In the 50% rated output dc voltage of Fig. 11(b), the ZVS is achieved at light load when the HB mode is applied. Moreover, the converter loss at light load is reduced by up to 62.3% due to the operation mode changing from FB to HB mode. In order to achieve the high efficiency in wide load, the two operation modes are changed at the output power of 500 W.

Fig. 12 shows the loss distribution of the each operation mode at the voltage condition of V_{in} = 400 V and V_{out} = 100 V in terms of calculated MOSFET losses using the datasheets of the HV- and LV-side MOSFETs. In this loss analysis, the losses of the magnetic component were obtained from the modeling software Gecko MAGNETICS [17]. In this software, the iron loss is calculated by using the improved-improved generalized steinmetz equation and improved generalized steinmetz equation [18]. The copper loss with the skin and proximity effects is considered in Gecko MAGNETICS [19]. In Fig. 12, the switching loss and the conduction loss with HB

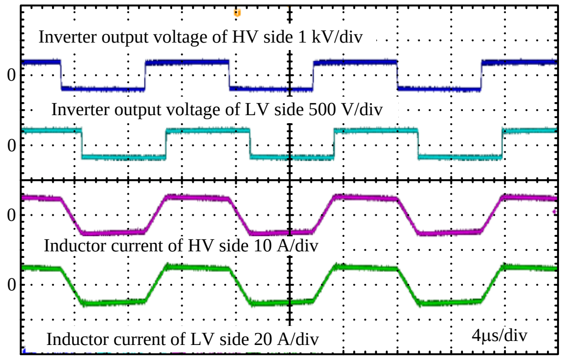

Fig. 8. Operation waveform at rated power of 1.5 kW, V_{in} = 400 V, V_{out} = 200 V

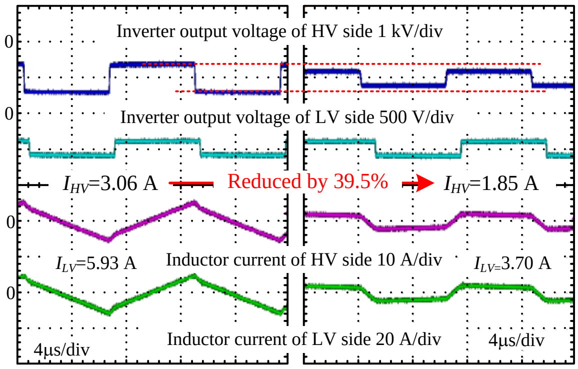

(a) FB mode at P_{out} = 350 W (b) HB mode at P_{out}= 350 W

Fig. 9. Operation waveforms with each mode at V_{in}=400 V, V_{out}=100 V and 23.3%.

mode are much lower than that with FB mode due to the ZVS achievement and the reduction of the inductance current at the switching timing. However, the conduction loss of HV side is increased because the bidirectional switch in the prototype is used with two MOSFET. In order to improve the prototype efficiency, the switching device which has a lower on-resistance will be selected.

C. Voltage control with operation mode changing

Fig. 13 shows the transient response at the load step change. This test is conducted with the load step change from 150 W to 750 W. Fig. 13(a) and (c) shows the transient response with the only FB mode, whereas Fig. 13(b) and (d) shows that with the operation mode changing. In Fig. 13(a) to (d), the dc offset of the inductor current is eliminated at the operation mode changing and the phase-angle command shifting. In Fig. 13(b) and (d), the undershoot, overshoot voltage, and the settling times are 19 V, 24 V, 1.40 ms, and 2.17 ms, respectively. The maximum error ratio which is compared to only FB mode is 7.0%. Therefore, the response of the proposed voltage control with changing the operation mode is similar to that with only FB mode because the nonlinearity in the current-control characteristic is compensated by the reverse system model regardless of the operation mode.

V. Conclusion

This paper proposed the voltage control method for the one-leg TDAB converter in order to achieve the linearization

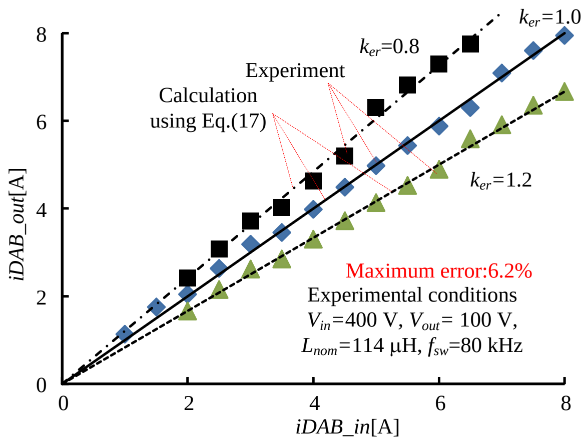

(a) FB mode

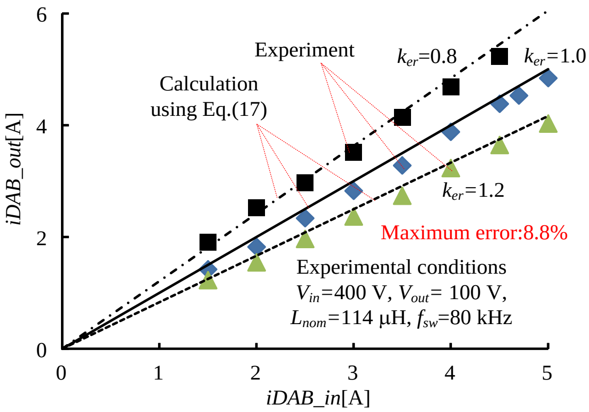

(b) HB mode

Fig. 10. Reference and output current characteristics of one-leg TDAB converter. The ratio between the output current command and the actual output current agrees with the calculation value regardless of the operation mode.

of the current-control characteristic and the elimination of the dc offset of the inductor current at the transient state. The one-leg TDAB converter with the proposed method contributed the voltage controller with the simple controller design. As the experiment results, the converter loss at half of the rated voltage condition was reduced by up to 62.3%. Besides, the ratio between the output current command and the actual output current agreed with the inductance error ratio, i.e. the maximum error of 8.8%. In addition, the load step response was confirmed without the dc offset of the inductor current when the phase-shift angle and the operation mode were changed. In future work, the converter efficiency will be improved by the optimizing design of the switching devices and the magnetic component.

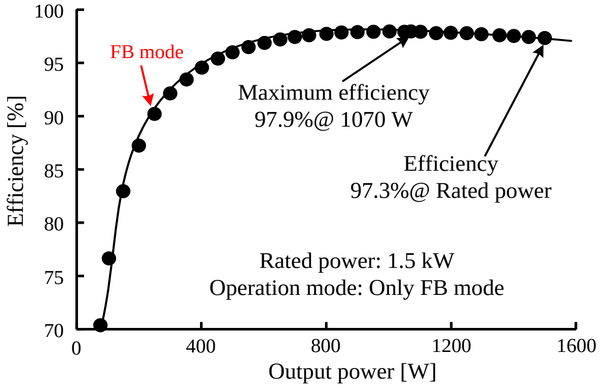

(a) V_{in} = 400 V, V_{out} = 200 V, NV_{out}/V_{in}=1.0

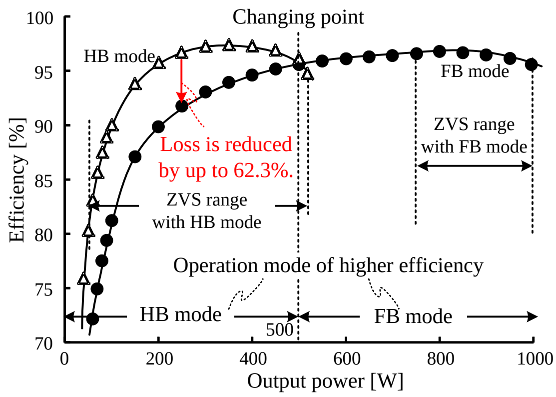

(b) V_{in}=400 V, V_{out}=100 V, NV_{out}/V_{in}=0.5

Fig. 11. Efficiency characteristic of each mode at input voltage of 400 V. The maximum efficency of 97.9% is ahchieved. In addition, the converter loss is reduced by up to 62.3% as shown in (b).

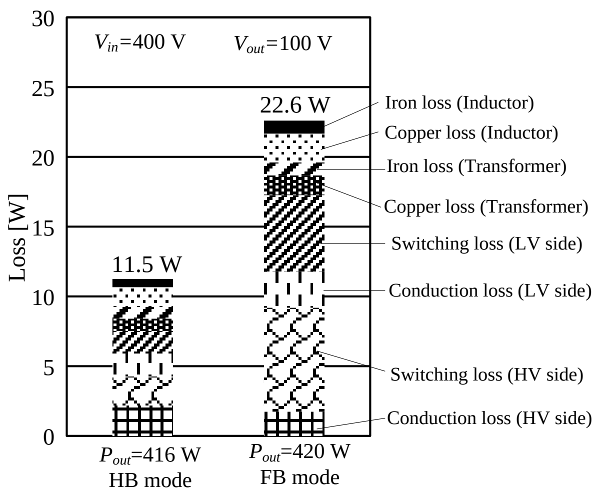

Fig. 12. Loss distribution of each mode at voltage condition of V_{in} = 400 V, V_{out}=100 V. By using HB mode, the switching loss with HV- and LV-side are reduced. Besides, the HV-side conduction loss is predominant in HB mode.

References

[1] T. Dragičević, X. Lu, J. C. Vasquez, and J. M. Guerrero, "DC Microgrids- Part II: A Review of Power Architectures, Applications, and Standardization Issues," *IEEE Transactions on Power Electronics*, vol. 31, no. 5, pp. 3528–3549, 2016.

[2] D. J. Becker and B. J. Sonnenberg, "DC Microgrids in Buildings and Data Centers," in *Conf. Proc. of IEEE Intern. Telecommunications Energy Conference INTELEC*, pp. 1-7, 2011.

[3] Y. Yu, K. Masumoto, K. Wada, and Y. Kado, "A DC Power Distribution System in a Data Center using a Triple Active Bridge DC-DC Converter," *IEEJ Journal. Industry Applications*, vol. 7, no. 3, pp. 202-209, 2018.

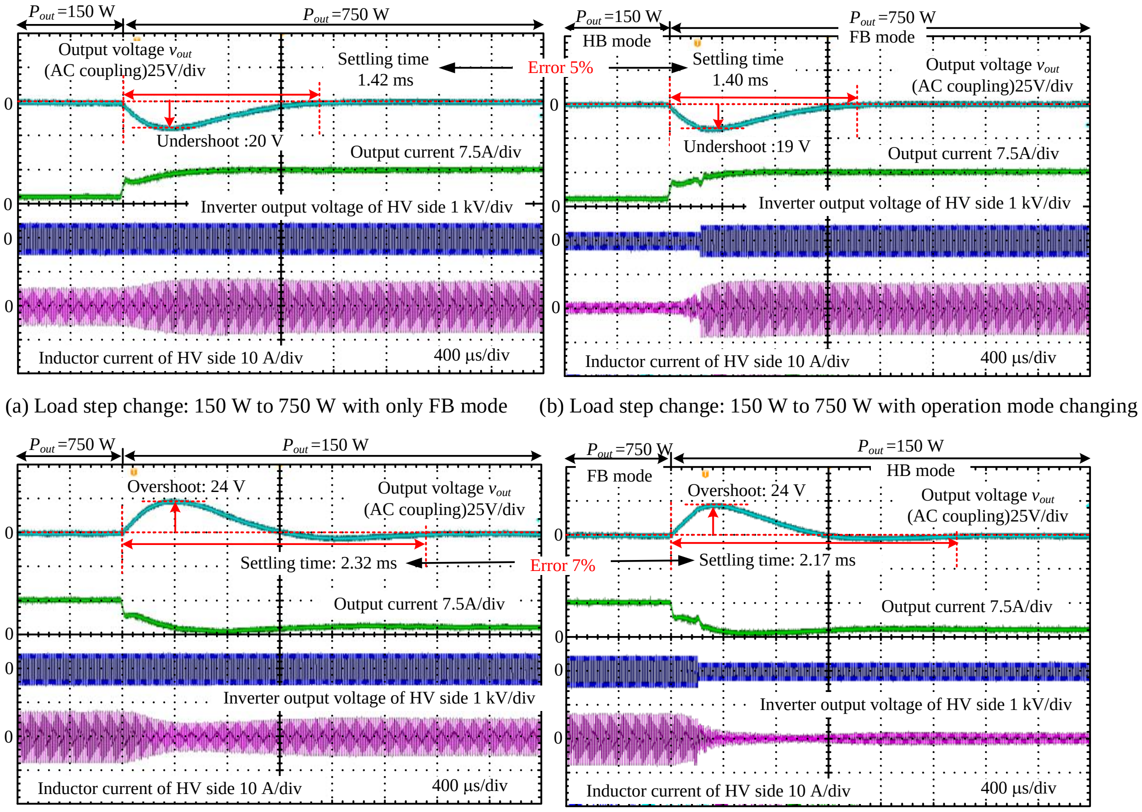

(a) Load step change: 150 W to 750 W with only FB mode (b) Load step change: 150 W to 750 W with operation mode changing

(c) Load step change: 750 W to 150 W with only FB mode (d) Load step change: 750 W to 150 W with operation mode changing

Fig. 13. Load transient response by output voltage control with only FB mode or operation mode changing. The undershoot, overshoot voltage, and the settling times are 19 V, 24 V, 1.40 ms, and 2.17 ms, respectively. The maximum error ratio which is compared to only FB mode is 7.0%. As a result, the response of the proposed voltage control with the operation mode changing is similar to that with only FB mode because the nonlinearity in the current-control characteristic is compensated by the reverse system model regardless of the operation mode.

[4] K. Kurohane, T. Senjyu, A. Yona, N. Urasaki, E.B. Muhando, and T. Funabashi, "A High Quality Power Supply System with DC Smart Grid," in *Conf. Proc. of Transmission and Distribution Conference and Exposition, 2010 IEEE PES*, pp.1-6, 2010.

[5] M. H. A. b. A. Malek, H. Kakigano, and K. Takaba, "Combined Pulse-Width Modulation of Dual Active Bridge DC-DC Converter to Increase the Efficiency of Bidirectional Power Transfer," *IEEJ J. Industry Applications*, vol. 7, no. 2, pp. 166-174, 2018.

[6] R. W. D. Doncker, D. M. Divian, and M. H. Kheraluwala, "A three-phase soft-switched high-power-density dc/dc converter for high-power applications," *IEEE Transactions on Industry Applications*, vol, 27, no. 1, pp. 63-73, 1991.

[7] M. N. Kheraluwala, R. W. Gascoigne, D. M. Divan, and E. D. Baumann, "Performance Characterization of a High Power Dual Active Bridge dc-to-dc Converter," *IEEE Transactions on Industry Applications*, vol. 28, no. 6, pp. 1294-1301, 1992.

[8] S. Inoue, and H. Akagi, "A bidirectional isolated dc–dc converter as a core circuit of the next-generation medium-voltage power conversion system," *IEEE Transactions on Industry Applications*, vol. 22, no. 2, pp. 535-542, 2007.

[9] P. A. M. Bezerra, F. Krismer, R, M. Burkart, and J. W. Kolar, "Bidirectional Isolated Non-Resonant DAB DC–DC Converter for Ultra-Wide Input Voltage Range Applications," in *Conf. Proc. of 2014 International Power Electronics and Application Conference and Exposition*, pp. 1038-1044, 2014.

[10] G. E. Sfakianakis, J. Everts, H. Huisman, and E. A. Lomonova, "ZVS modulation strategy for a 3-5 level bidirectional Dual Active Bridge DC -DC converter," in *Conf. Proc. of 2016 Eleventh International Conference on Ecological Vehicles and Renewable Energies*, pp. 1-9, 2016.

[11] H. Higa, S. Takuma, K. Orikawa, and J. Itoh, "Dual active bridge DC-DC converter using both full and half bridge topologies to achieve high efficiency for wide load," in *Conf. Proc. of 2015 IEEE Energy Conversion Congress and Exposition*, pp. 6344-6351, 2015.

[12] Guo Xu, Deshang Sha, Yaxiong Xu, and Xiaozhong Liao, "Hybrid-Bridge-Based DAB Converter with Voltage Match Control for Wide Voltage Conversion Gain Application," *IEEE Transactions on Power Electronics*, vol. 33, no. 2, pp. 1378-1388, 2018.

[13] G. E. Sfakianakis, J. Everts, H. Huisman, T. Borrias, C. G. E. Wijnands, and E. A. Lomonova, "Charge-based ZVS modulation of a 3–5 level bidirectional dual active bridge DC-DC converter," in *Conf. Proc. of 2016 IEEE Energy Conversion Congress and Exposition*, pp. 1-10, 2016.

[14] K. Takagi, and H. Fujita, "Dynamic Control and Dead-Time Compensation Method of an Isolated Dual-Active-Bridge DC-DC Converter," in *Conf. Proc. of 2015 European Conference on Power Electronics and Applications* , pp. 1-10, 2015.

[15] H. Fujita, S. Tominaga, and H. Akagi, "Analysis and design of a dc voltage-controlled static var compensator using quad series voltage-source inverters," *IEEE Transactions on. Industry Applications*, vol.32, no. 4, pp.970-977, 1996.

[16] M. Kasper, R. Burkart, G. Deboy, and J. W. Kolar, "ZVS of Power MOSFETs Revisited," *IEEE Transactions on Power Electronics*, vol. 31, no. 12, pp. 8063-8067, 2016.

[17] [Online] http://gecko-simulations.com/geckomagnetics.html.

[18] J. Mühlethaler, J. W. Kolar, and A. Ecklebe, "Loss Modeling of Inductive Components Employed in Power Electronic Systems," in *Conf. Proc. of ECCE Asia 2011 (ICPE)*, pp. 945-952, 2011.

[19] J. M¨uhlethaler, "Modeling and Multi-Objective Optimization of Inductive Power Components," *Ph.D. dissertation*, ETH Zurich, 2012.